

Strong anisotropy in the mixed antiferromagnetic system $\text{Mn}_{1-x}\text{Fe}_x\text{PSe}_3$

Ankita Bhutani,¹ Julia L. Zuo,¹ Rebecca D. McAuliffe,¹ Clarina R. dela Cruz,² and Daniel P. Shoemaker¹

¹*Materials Science and Engineering Department and Materials Research Laboratory,
University of Illinois at Urbana-Champaign, Urbana, Illinois, USA.*

²*Neutron Scattering Division, Oak Ridge National Laboratory, Oak Ridge, TN 37831, United States*
(Dated: March 3, 2020)

We report the magnetic phase diagram of $\text{Mn}_{1-x}\text{Fe}_x\text{PSe}_3$ which represents a random magnet system of two antiferromagnetic systems with mixed spin, mixed spin anisotropies, mixed nearest neighbor magnetic interactions and mixed periodicities in their respective antiferromagnetic structure. Bulk samples of $\text{Mn}_{1-x}\text{Fe}_x\text{PSe}_3$ have been prepared and characterized phase pure by powder X-ray and neutron diffraction and X-ray fluorescence. Nature and extent of magnetically ordered state has been established using powder neutron diffraction, dc magnetic susceptibility and heat capacity. Long-range magnetic ordering exists between $x = 0.0$ and 0.25 (MnPSe_3 -type) and between $x = 0.875$ and 1 (FePSe_3 -type). A short-range magnetic order with existence of both MnPSe_3 - and FePSe_3 -type nano-clusters has been established between $x = 0.25$ and 0.875 . Irreversibility in dc magnetization measurements, also characterized by isothermal and thermoremanent magnetization measurements suggest similarities to magnetic nanoparticles where uncompensated surface spins result in diverging thermoremanent and isothermal remanent magnetization responses, further reinforcing existence of magnetic nano-clusters or domains. A spin glass state, observed in analogous $\text{Mn}_{1-x}\text{Fe}_x\text{PS}_3$, has been ruled out and formation of nano-clusters exhibiting both ordering types results from unusually high anisotropy values. The effect of ligand contributions to the spin-orbit interactions has been suggested as a possible explanation for high D values in these compounds.

I. INTRODUCTION

Disrupting the long-range ordering of magnetic systems can manifest a variety of behaviors in crystalline materials, perhaps most notably in the form of emergent properties such as unconventional superconductivity in iron-based and cuprate materials. In those cases, the spin interactions are complex, with a mixture of local and itinerant moments and quantum fluctuations, respectively, leading to complex behavior. The superconducting parent compounds could be contrasted with materials where the behavior is more pedestrian, such as strongly classical systems where spin-glass behavior arises as multiple competing order parameters lead to a frozen state. A third, uncommon scenario can occur when the local coupling is strong enough to preclude the spin glass state, and competition can lead to uncompensated moments via complex domain formation.

A detailed mean-field and renormalization-group study of the possible magnetic orderings of randomly-mixed magnets was conducted by Fishman and Aharony in 1978.¹⁻³ A random magnet containing a mixture of ions with competing spin anisotropies orders in a “mixed phase” or “oblique antiferromagnetic phase” at intermediate compositions and the phase diagram of such a magnet exhibits a tetracritical “decoupled” point. Experimental evidence of such phases has been observed in the solid-solution intermetallic $\text{Tb}_x\text{Er}_{1-x}\text{Ni}_5$ and ionic $\text{Fe}_{1-x}\text{Co}_x\text{Cl}_2$.^{4,5} On the other hand, mixtures of antiferromagnets with different periodicities can form an intermediate phase with both magnetic orderings, as observed in $\text{Fe}_{1-x}\text{Mn}_x\text{WO}_4$.⁶ A random magnet with competing interactions forms a disordered or spin glass state as observed in $\text{Mn}_{1-x}\text{Fe}_x\text{PS}_3$.⁷

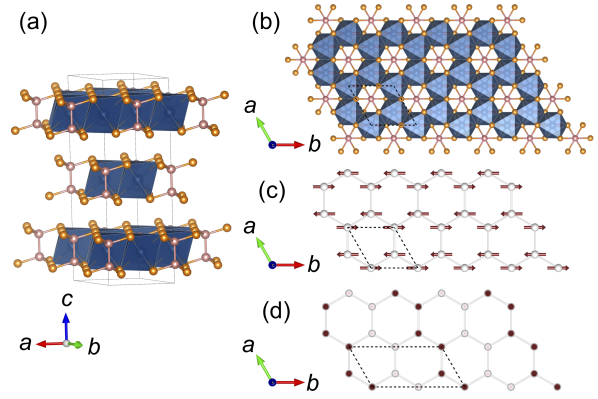


Figure 1. (a) Atomic structure of MPSe_3 for $M = \text{Mn}$ or Fe , with transition metals in dark blue octahedra, P (pink) and Se (orange). In (b), a single layer of the structure is shown with the $k = 0$ magnetic cell of MnPSe_3 dashed. The honeycomb pattern arises from periodic P_2Se_6 polyanions, where pairs of P are eclipsed in this view. The magnetic structure of MnPSe_3 is shown in (c), with Mn^{2+} only in white. Spins are in the ab plane. In (d), the magnetic structure of FePSe_3 is shown, with spins pointing in the $\pm c$ direction. (b-d) are shown at the same scale. The direction of the Mn^{2+} moments in the basal plane was recently found to be canted 8° from b .⁸

$\text{Fe}_{1-x}\text{Mn}_x\text{WO}_4$ displays a very rich magnetic phase diagram where MnWO_4 exhibits 3 types of antiferromagnetic ordering and FeWO_4 exhibits only 1 type. A solid solution between the two results in competition between and a coexistence of interpenetrating magnetic structures related to the pure systems MnWO_4 and FeWO_4 .

Two such compounds that exhibit different magnetic interactions and orderings are MnPSe_3 and FePSe_3 be-

longing to the family of metal thio(seleno)phosphates (MTPs), which are two-dimensional layered compounds with layers bound by weak van der Waals forces. MTPs form a unique family of compounds in which the spin dimensionality may be varied by the choice of the transition metal ion. The MTPs were first discovered by Friedel in 1894.⁹ MnPSe_3 and FePSe_3 are isostructural and crystallize in the $R\bar{3}$ space group. $\text{M}_2\text{P}_2\text{Se}_6$ can be visualized as $ABCABC$ -stacked slabs of CdI_2 -like units with 2/3 of the edge-sharing octahedral centers occupied by the transition metal cations, forming a honeycomb network, and the remaining 1/3 occupied by the P-P dimers as shown in Figure 1. P-P dimers covalently bond to six Se atoms to form $(\text{P}_2\text{Se}_6)^{-4}$ ethane-like polyanion units.

The magnetic structures for MnPSe_3 and FePSe_3 were first examined in 1981 using neutron powder diffraction by Wiedenmann, *et al.*¹⁰ MnPSe_3 and FePSe_3 both order antiferromagnetically with T_N of 74 and 119 K and Néel vectors $k = [000]$ and $k = [1/2\ 0\ 1/2]$, respectively. Layers of both magnetic structures are plotted in Figure 1(c,d). The magnetic moments of Mn^{2+} ($S = 5/2$) lie in the basal plane all three intralayer $J1$ (n), $J2$ (nn) and $J3$ (nnn) interactions are antiferromagnetic. On the other hand, the magnetic moments of Fe^{2+} ($S = 2$) lie along c -axis with $J1$ being ferromagnetic, and $J2$ and $J3$ being antiferromagnetic. MnPSe_3 and FePSe_3 can thus be represented as Heisenberg XY and Ising systems, respectively. A solid solution between MnPSe_3 and FePSe_3 thus represents a quite complex random alloy, where S , J , D and k are all competing. Such a competition can result in presence of one or more of the theoretically predicted and experimentally realized magnetically ordered phases depending on the chemical composition. Magnetic ordering can, therefore, either be glassy in case of strong competing exchange interactions as observed in sulfides, or be a competing two-phase ordered state in case of strong anisotropic contributions to the total Hamiltonian.

In this article, we present a detailed investigation of the magnetic phase diagram of $\text{Mn}_{1-x}\text{Fe}_x\text{PSe}_3$ by means of X-ray diffraction, X-ray Fluorescence, powder neutron diffraction, DC magnetization and heat capacity measurements. Our investigation reveals presence of the two end-member magnetic orderings along with a region of competing antiferromagnetic orders that exhibits uncompensated moments and nanoscale domains, as evidenced by broad magnetic diffraction peaks, despite sharp structural Bragg peaks.

II. EXPERIMENTAL PROCEDURE

Bulk synthesis of the samples in the solid solution range of $\text{Mn}_{1-x}\text{Fe}_x\text{PSe}_3$ ($0 \leq x \leq 1$, in increments of 0.125) was carried out using traditional solid state synthesis. Reagents of Mn (crushed granules, Alfa Aesar, 99.98%), Fe (200 mesh, Alfa Aesar, 99%), P (red, powder, Sigma-Aldrich, 99.99%), and Se (crushed granules, Alfa Aesar, 99.999%) were ground together in an Ar-filled glove box.

Precursors were loaded in 12 mm diameter fused silica tubes and sealed under vacuum using liquid nitrogen to prevent P and Se loss during vacuum sealing, and reacted at 650°C with a ramp rate of 10°C per minute and 30 days hold time, followed by furnace cooling. Heating at higher temperatures led to decomposition of the product, and no large crystals were obtained.

Powder X-ray diffraction measurements were conducted in transmission with a Bruker D8 diffractometer with $\text{Mo-K}\alpha$ radiation. Rietveld analysis was carried out using TOPAS 5.¹¹ XRF data were collected using a Shimadzu EDX-7000 spectrometer under a He atmosphere. Three sets of data were collected and averaged to determine the composition.

Neutron diffraction data were collected between 1.5 K and 300 K using the HB-2A powder diffractometer at the High Flux Isotope Reactor at Oak Ridge National Laboratory for $x = 0, 0.25, 0.375, 0.5, 0.625$ and 1. Powders (1-2 g) were loaded in V cans with He exchange gas and measured with incident neutrons with wavelength $\lambda = 2.41$ Å. Rietveld analyses and magnetic structure solutions were performed with FullProf and SARAh.^{12,13}

Magnetic susceptibility measurements were collected on a Quantum Design MPMS 3 magnetometer. Thermoremanent magnetization (TRM) and isothermal remanent magnetization (IRM) measurements were also collected on a Quantum Design MPMS 3 magnetometer.

The samples were field-cooled to 5 K, the temperature was stabilized for 10 min, field was turned off and the remanent moment was measured at the varying fields. For IRM measurements, the samples were cooled in zero field to 5 K, the temperature was stabilized for 10 min, a magnetic field was applied for 10 min and switched off, and remanent magnetic moment was measured. Heat capacity measurements were performed using a Quantum Design Dynacool PPMS (Physical Property Measurement System), with pressed pellets mounted using N-grease and a two-tau procedure.

III. RESULTS AND DISCUSSION

A. Evaluating structure and long-range order

Laboratory powder X-ray diffraction patterns for all compositions in $\text{Mn}_{1-x}\text{Fe}_x\text{PSe}_3$ at room temperature are shown in Figure 2. The Rietveld refinements for the diffraction patterns indicate that all synthesized compositions are phase pure. Due to the long annealing times (30 days) and the consistent peak width of reflections at high Q , it is apparent that the cation ordering is random and relaxed. However, the occupancies of Mn and Fe are indistinguishable by X-ray diffraction analysis and were refined separately by neutron diffraction. The Mn/Fe ratios obtained from XRF data are plotted in Figure 3 and slightly overestimate the Fe content by less than 10%. The XRD-refined chemical contraction of the unit cell from MnPSe_3 to FePSe_3 varies smoothly, with a total

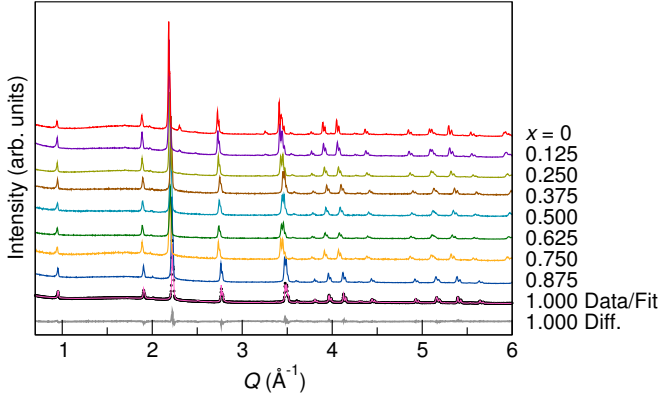


Figure 2. Room-temperature X-ray diffraction patterns of $\text{Mn}_{1-x}\text{Fe}_x\text{PSe}_3$ show consistent formation of the same structure type, without impurities, and with consistent peak width. The refinement to the FePSe_3 end member with the difference curve is shown.

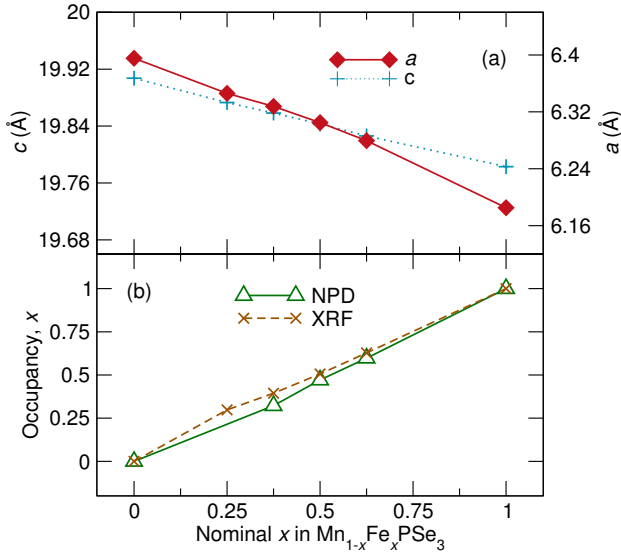


Figure 3. Lattice parameters (a) refined from neutron diffraction data show linear variations from Mn/Fe substitution, with $R\bar{3}$ space group. In (b), agreement within 5% is seen in the neutron-refined Mn/Fe occupancies and the Mn/Fe ratio obtained from XRF. Taken together, the data indicate a random solid solution. Error bars are smaller than symbols in all cases.

change of about 4% in a and 2% in c . This provides a consistent picture that the individual samples are truly a solid solution.

Magnetic susceptibility measurements for all compositions in $\text{Mn}_{1-x}\text{Fe}_x\text{PSe}_3$ are shown in Figure 4. For low-dimensional systems, the value of T_N as measured by specific heat is not always directly correlated to the maximum in the susceptibility versus T , and a broad maximum above T_N is caused by short-range spin correlations.^{14–17} Here the T_N from heat capacity (Figure 5) is more closely tracked by the point where the slope of

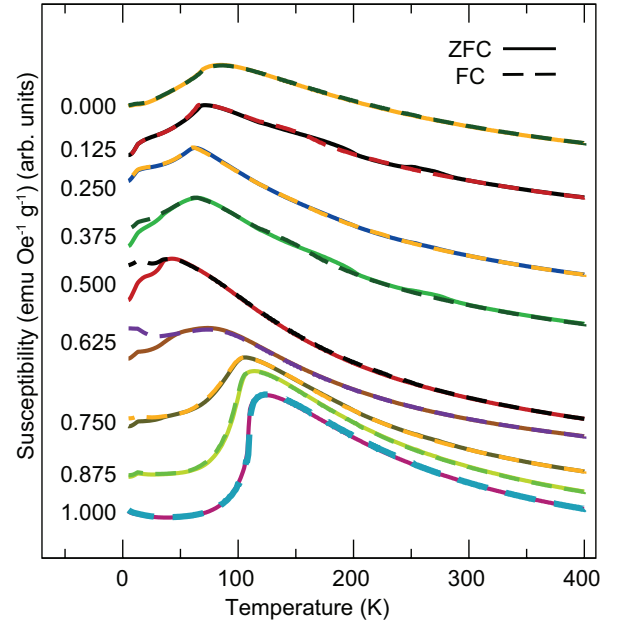


Figure 4. Magnetic susceptibility under zero-field cooling and field cooling with $H = 100$ Oe for all samples in the $\text{Mn}_{1-x}\text{Fe}_x\text{PSe}_3$ range. The most apparent proxy for Neel temperature is the maximum in susceptibility T_{max} , evident for each curve. Only samples from $x = 0.375$ to 0.625 show irreversibility, as evidenced in deviation of the ZFC and FC susceptibilities.

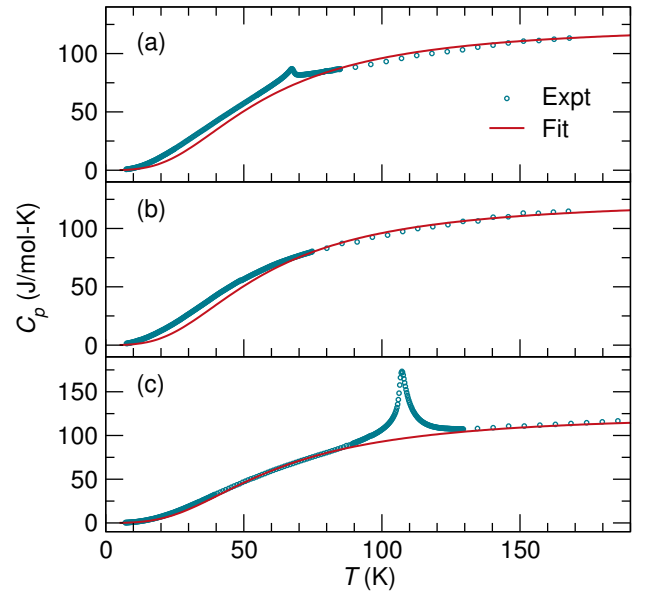


Figure 5. Heat capacity of the end members (a) MnPSe_3 and (c) FePSe_3 display clear peaks at the first-order T_N . The peak in MnPSe_3 is weaker due to the lack of orbital contribution when $S = 5/2$. At $x = 0.5$ in (b), the transition is broadened due to slow growth of nano-sized competing magnetic domains, but the total contribution can still be extracted from the Debye fits.

the $\chi - T$ curve is maximized. The heat capacity of the $x = 0.5$ sample shows no lambda anomaly, although the general features of the susceptibility vary smoothly with x .

Curie-Weiss temperatures θ and effective magnetic moments (μ_{eff}) were extracted from the susceptibility over the 280-400 K temperature range. The θ values are negative and summarized in Table I, indicating short-range antiferromagnetic interactions in all compositions, and quite strong $\theta = -146$ K in MnPSe_3 , which gradually weakens with Fe substitution. The effective magnetic moments μ_{eff} of MnPSe_3 ($5.9\mu_B$) and FePSe_3 ($5.2\mu_B$) indicate that both Mn^{2+} and Fe^{2+} are present in a high-spin state with $S = 5/2$ and $S = 2$. The μ_{eff} of all compounds agree roughly with the ideal values, except for the $x = 0.875$ and $x = 1$ samples, where T_{max} is sufficiently high that strict adherence to Curie-Weiss behavior is not expected below 400 K.

Splitting between the ZFC and FC susceptibilities in Figure 4 is only observed from $x = 0.375$ to $x = 0.75$ and occurs around 40 K. The onset of this irreversibility is denoted T_{split} in Table I and suggests uncompensated spins that arise at boundaries of domains with dissimilar magnetic orderings, so it is not evident in the end members. The uncompensated surface spins of the domains can behave in a glassy or disordered way. The highest degree of irreversibility is observed as x approaches 0.5 suggesting a higher uncompensated surface contribution from magnetic domains in intermediate compositions.

The total heat capacity measurements in Figure 5 only display an obvious λ anomaly for the end members MnPSe_3 and FePSe_3 , but even fitting the $x = 0.5$ sample to the Debye model reveals a gradual onset of magnetic ordering. The large peak in FePSe_3 (compared to MnPSe_3) can be explained by the magnetoelectric contribution from spin-orbit coupling, as was suggested for FePS_3 .¹⁸ Furthermore, the magnetic frustration as viewed by a larger Curie-Weiss θ versus the susceptibility T_{max} indicates that MnPSe_3 is frustrated, and slowly orders with increasing domain size upon cooling. This is reflected in the deviation of C_p versus the Debye fit in Figure 5(a).

The total heat capacity at low temperatures is a combination of electronic, lattice and magnetic contributions $C_{\text{total}} = C_{\text{elec}} + C_{\text{lat}} + C_{\text{mag}}$, where C_{elec} is γT , C_{lat} is $\beta T^3 + \alpha T^5$. The fit to the heat capacity at low temperatures (7 – 10 K) was made using C_{lat} since these chalcogenides are insulators with high resistivity of the order of $10^6 \Omega\text{-m}$ to estimate Debye temperatures. The high-temperature heat capacity data was then fit using the Debye model to better estimate C_{lat} and Debye temperatures. C_{mag} was calculated by $C_{\text{total}} - C_{\text{lat}}$ and C_{mag}/T vs T plot was integrated to give the entropy associated with the magnetic transition. The theoretical limit to the statistical magnetic entropy for complete ordering of Mn^{2+} ($S = 5/2$) should be $R \ln(2S + 1) = 14.89 \text{ J mol}^{-1} \text{ K}^{-1}$ and of Fe^{2+} ($S = 2$) should be $13.38 \text{ J mol}^{-1} \text{ K}^{-1}$. It is clear from Figure 5 that the

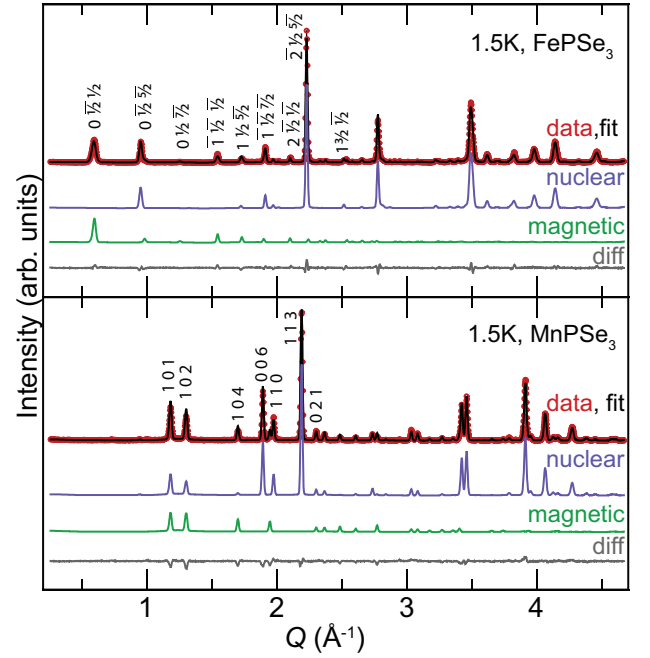


Figure 6. Refinements to neutron powder diffraction data at $T = 1.5$ K for FePSe_3 and MnPSe_3 show clear signatures from magnetic ordering. All magnetic intensity in MnPSe_3 lies on nuclear reflections since $k = [000]$.

$\text{Mn}_{1-x}\text{Fe}_x\text{PSe}_3$ does precisely track Debye-like behavior, as is typical for similar materials,¹⁹ but rough agreement is seen: The entropy calculated for $x = 0, 0.5$ and 1.0 amount to $13.84 \text{ J mol}^{-1} \text{ K}^{-1}$, $13.23 \text{ J mol}^{-1} \text{ K}^{-1}$ and $10.73 \text{ J mol}^{-1} \text{ K}^{-1}$ with respective Debye temperatures of 235 K, 240 K and 250 K. These values indicate that the ordering in intermediate compositions is still transitioning from states that are nearly fully disordered to fully ordered over the measured temperature range.

B. Progression of magnetic ordering across the $\text{Mn}_{1-x}\text{Fe}_x\text{PSe}_3$ compositional range

Our refined neutron powder diffraction data at $T = 1.5$ K is shown for the end members MnPSe_3 and FePSe_3 in Figure 6. We verify the magnetic propagation vectors $k = [000]$ and $k = [\frac{1}{2}0\frac{1}{2}]$, respectively.¹⁰ The average magnetic moments on Mn^{2+} and Fe^{2+} in the end members were refined to $3.6 \mu_B$ and $4.2 \mu_B$, respectively. The in-plane direction of the Mn^{2+} moments cannot be determined from powder neutron scattering due to the hexagonal $R\bar{3}$ symmetry.

The smaller magnitudes of neutron-refined magnetic moments versus the paramagnetic moments from susceptibility can be attributed to uncertainty in the canting of magnetic moments or to small domain sizes with imperfect magnetic ordering in MnPSe_3 . The magnetic structures of the analogous sulfides remain a topic of active investigation.^{8,20} The magnetic structure of MnPS_3 was

Table I. Expected values and measured parameters from magnetic susceptibility measurements and fits to Curie-Weiss behavior (μ_{eff} and θ).

x in $\text{Mn}_{1-x}\text{Fe}_x\text{PSe}_3$	S_{ideal}	$\mu_{\text{eff,ideal}} (\mu_B)$	$\mu_{\text{eff,expt}} (\mu_B)$	θ (K)	T_{max} (K)	T_{split} (K)
0.000	5/2	5.92	5.90	-146	84	-
0.125	2.44	5.79	5.98	-150	70	-
0.250	2.38	5.66	5.98	-130	61	-
0.375	2.31	5.54	5.68	-97.7	63	40
0.500	2.25	5.41	5.76	-88.6	40	40
0.625	2.19	5.28	4.82	-56.6	73	46
0.750	2.13	5.15	4.93	-39.7	105	43
0.875	2.06	5.03	5.43	-28.3	113	-
1.000	2.00	4.90	5.24	-8.86	124	-

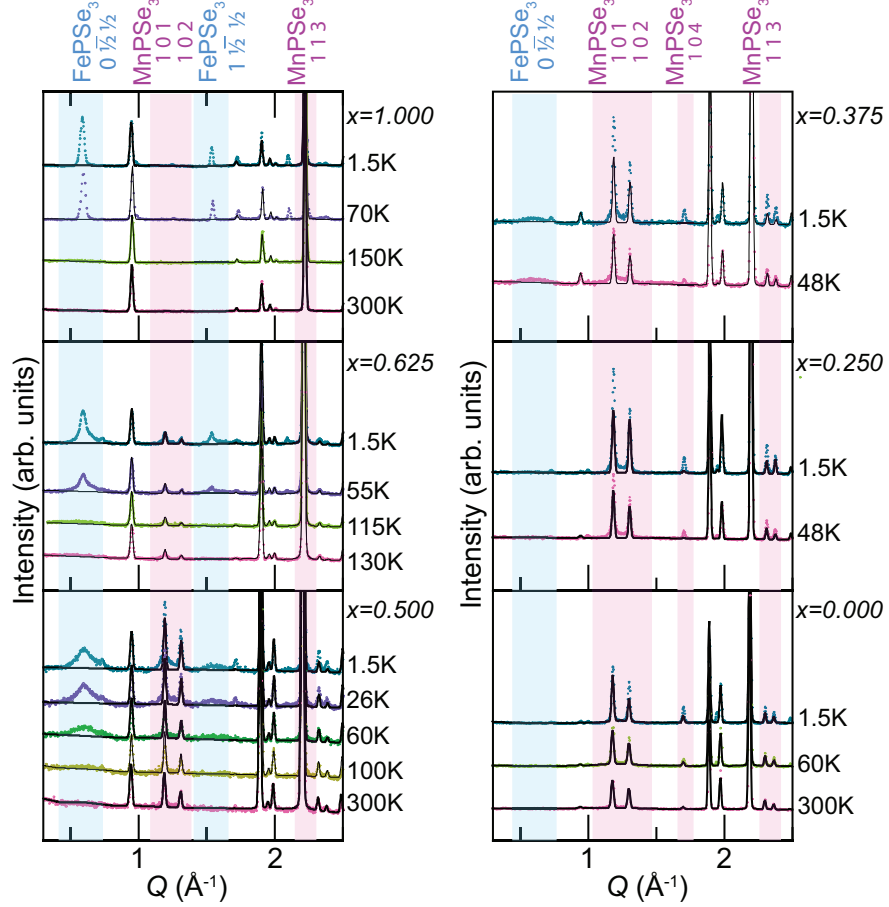


Figure 7. Evolution of magnetic ordering peaks with temperature and composition. The nuclear fits have been shown in black to clearly identify magnetic intensities at various temperatures. Peaks corresponding to FePSe_3 -type and MnPSe_3 -type magnetic ordering have been highlighted in blue and pink respectively. Presence of broad diffuse magnetic peaks caused by short-range order is seen in intermediate compositions as compared to sharp magnetic peaks in end members.

identified with a propagation vector of $k = [000]$ where the Mn^{2+} moments lie at an angle of 8° from the c^* axis, as compared to the previously-published magnetic structure where the magnetic moments are along c^* .⁸ If MnPSe_3 also has a canted configuration, Rietveld analysis with Mn^{2+} moments lying in the ab plane would cause the calculated magnetic moments to be lower than the true value. On the other hand, small magnetic corre-

lation lengths in MnPSe_3 are shown in Figure 9, indicating a lack of perfect long-range magnetic ordering. The prevalence of disordered regions between these domains would also lead to a smaller neutron-refined magnetic moment.

Across the compositional range, a few key changes should be noted in the neutron diffraction patterns at 1.5 K, shown in Figure 7: first, the magnetic reflections

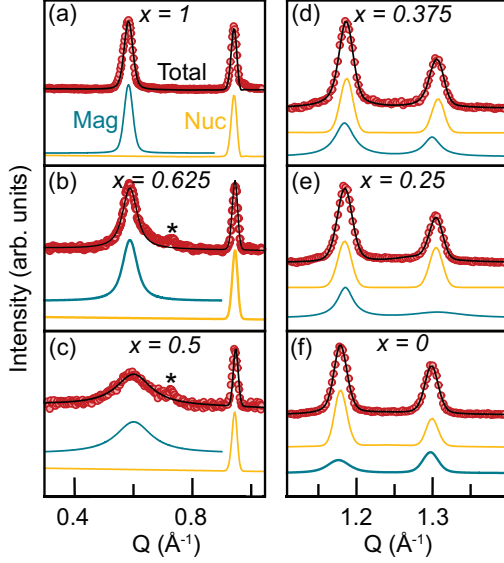


Figure 8. Magnetic and nuclear contributions obtained from Rietveld refinements of neutron diffraction patterns at 1.5K for (a) $x = 1$, (b) 0.625, (c) 0.5, (d) 0.375, (e) 0.25, and (f) 0. A minor peak marked with an asterisk is assumed to be a magnetic peak from Fe_7S_8 that was below the detection level of our XRD data.

in FePSe_3 are clearly broadened (and although it is more subtle, there is substantial diffuse scattering from magnetic intensity in MnPSe_3), and there is a progression of mixing and broadening of the magnetic Bragg contributions from both phases as intermediate values of x are examined.

In FePSe_3 , the broadening of the $0\frac{1}{2}\frac{1}{2}$ magnetic reflection is not immediately apparent from Figure 6, but upon closer inspection in Figure 8, it is significant and can be refined as a Voigt contribution corresponding to a correlation length $L = 600 \pm 200 \text{ \AA}$, and remains broad at $T = 70 \text{ K}$ to $L = 500 \pm 100 \text{ \AA}$. This peak broadens further into a diffuse, but still detectable, contribution at 150 K, which is higher than $T_N = 124 \text{ K}$ for FePSe_3 , indicating short-range magnetic correlations that are common for low-dimensional materials.^{15–17} For a higher-angle $1\frac{1}{2}\frac{1}{2}$ magnetic peak, the correlation lengths are not determinable within the limits of instrumental and sample broadening.

In other magnetic compounds with strong crystalline anisotropy such as Sr_2YRuO_6 ²¹, CrTa_2O_6 ²² and $\text{La}_2\text{O}_3\text{Mn}_2\text{Se}_2$,²³ magnetic domains that exhibit strong correlations in two dimensions above 3D long range magnetic transition temperature are typically modeled by Warren-type peaks,²⁴ which are characterized by long tails with increasing Q , similar to turbostratic nuclear disorder in layered compounds and clays. While the layered structure of $\text{Mn}_{1-x}\text{Fe}_x\text{PSe}_3$ could play host to such disorder, we observe neither nuclear disorder nor Warren-type tails on the magnetic peaks. Instead, the magnetic peaks are best described as Lorentzian contributions af-

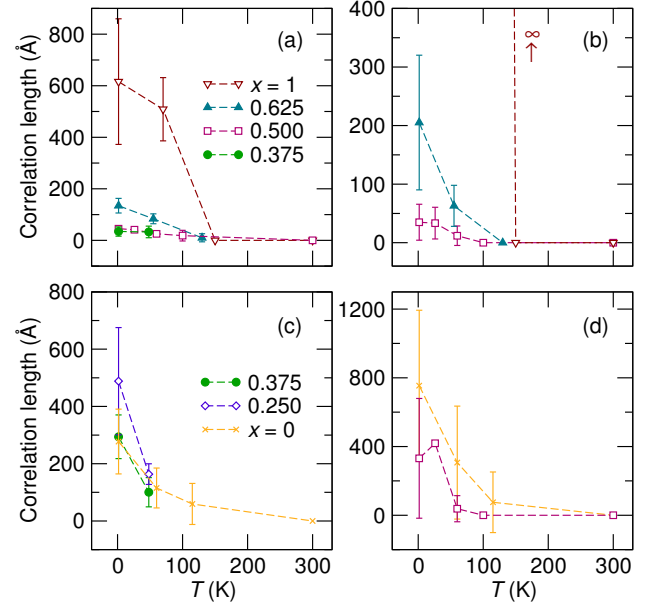


Figure 9. Magnetic correlation lengths for various compositions calculated as a function of temperature for (a) FePSe_3 -type $0\frac{1}{2}\frac{1}{2}$ at $Q = 0.6 \text{ \AA}^{-1}$, (b) FePSe_3 -type $1\frac{1}{2}\frac{1}{2}$ at $Q = 1.53 \text{ \AA}^{-1}$, (c) MnPSe_3 -type 101 at $Q = 1.17 \text{ \AA}^{-1}$ and (d) MnPSe_3 -type 102 at $Q = 1.30 \text{ \AA}^{-1}$.

ter instrumental and crystallite size corrections (Figure 8). This implies that the short range ordering present in $\text{Mn}_{1-x}\text{Fe}_x\text{PSe}_3$ has a significant interplane component, unlike other 2D materials such as Sr_2YRuO_6 , CrTa_2O_6 and $\text{La}_2\text{O}_3\text{Mn}_2\text{Se}_2$. This behavior is corroborated by the fact that the broad magnetic peaks correspond to hkl family of planes, instead of $hk0$.

For samples where $0.675 \leq x \leq 0.375$, magnetic peaks are broadened and the two k -vectors coexist. The extracted correlation lengths for these with varying composition and temperature are plotted in Figure 9. Interestingly, only the FePSe_3 end member at $x = 1$ shows domain sizes that are large enough that the peaks are not broadened versus the nuclear peaks. Correlation lengths drop more steeply for FePSe_3 -type ordering as compared to MnPSe_3 -type ordering for intermediate compositions. This could be explained by stronger anisotropic and hence less susceptible character of MnPSe_3 as compared to FePSe_3 .

C. Nature of and driving forces for the coexistence of magnetic domains

It is clear from the susceptibility and diffraction measurements that $\text{Mn}_{1-x}\text{Fe}_x\text{PSe}_3$ exhibit mixed magnetic ordering below T_N . The layers containing magnetic cations are separated by a van der Waals gap on the order of $\sim 7 \text{ \AA}$, which prohibits direct exchange and superexchange interactions between layers. The intralayer neighboring magnetic interactions are much stronger, as

evidenced by the non-Curie-Weiss behavior and diffuse magnetic scattering above T_N . Clearly, the differences between this system and other mixed magnets (which typically result in spin glasses) should be understood. For a random cation mixture on $\text{Mn}_{1-x}\text{Fe}_x\text{PSe}_3$, a Hamiltonian for the spin interactions can be written:

$$H = -2J_{Mn} - 2J_{Fe} - 2J_{MnFe} - D_{Mn} - D_{Fe}, \quad (1)$$

where,

$$\begin{aligned} J_{Mn} &= J_{MnMn} \sum_{\langle i,j \rangle} \vec{S}_{Mn_i} \cdot \vec{S}_{Mn_j}, \\ J_{Fe} &= J_{FeFe} \sum_{\langle k,l \rangle} \vec{S}_{Fe_k} \cdot \vec{S}_{Fe_l}, \\ J_{MnFe} &= J_{MnFe} \sum_{\langle p,q \rangle} \vec{S}_{Mn_p} \cdot \vec{S}_{Fe_q}, \\ D_{Mn} &= D_{Mn} \sum_i (S_{Mn_i}^z)^2, \\ D_{Fe} &= D_{Fe} \sum_k (S_{Fe_k}^z)^2 \end{aligned} \quad (2)$$

Here, J are exchange interactions between two neighboring magnetic ions and D denotes the anisotropy. $D_{Mn} < 0$ and $D_{Fe} > 0$ for MnPSe_3 and FePSe_3 as per their Heisenberg and Ising nature, respectively. MnPSe_3 is highly anisotropic as determined by single-crystal magnetic susceptibility measurements carried out by Jeevanandam²⁵ with a single-ion exchange anisotropy $D = 26.6$ K, which is approximately five times the exchange interaction (-5.29 K). No comparable susceptibility measurement exists for FePSe_3 to estimate the value of D . However, the exchange interaction J_{FeFe} is of similar magnitude (between 3.7 and 10.4 K) to that of MnPSe_3 but ferromagnetic as determined by Wiedenmann.¹⁰

At first glance, it may seem surprising that D_{Mn} is large, given the $3d^5$ electron configuration and zero orbital contribution. Magnetic anisotropy of Mn^{2+} compounds is perhaps best understood in the context of the MnX_2 halides where $X = (\text{F}, \text{Cl}, \text{Br}, \text{I})$. For the larger anions, covalency increases along with the ligand contribution to spin-orbit coupling. This increase in covalency, coupled with the highly anisotropic crystal structures of the halides (and the selenophosphates we investigate here) can be most dramatically observed in the magnetic anisotropy and in the strong photoluminescence and magnetic dichroism of MnI_2 .^{26,27} MnI_2 has the $\text{Cd}(\text{OH})_2$ structure type, with Mn in slightly trigonally-distorted octahedra, like MnPSe_3 , and without ligand covalency the observed optical transitions would be forbidden. A similar line of reasoning explains single-site anisotropy in Mn^{2+} single-molecule magnets²⁸ and the anisotropy in CrI_3 , which is also layered with a $3d^3$ ground state that possess magnetic anisotropy due to spin-orbit coupling.²⁹ Interplane ordering is more likely dipolar in nature.^{30,31} The treatment of spin-orbit-driven anisotropy in MnPSe_3 in particular has been laid out by Jeevanandam and

Vasuvedan.²⁵ Covalency and the spin-orbit coupling are both higher for selenium (1463 cm^{-1}) than for sulfur (1463 cm^{-1}),³² which in turn has a substantial effect on zero-field splitting parameter D . A more precise decomposition of the effects that lead to anisotropy in the chalcophosphates remains to be conducted, as the polyanionic species ($\text{P}_2\text{Se}_6^{4-}$) are not equivalent to selenides.

Assuming similar magnitudes of D_{Fe} and D_{Mn} , the question is what ordered states are accessible by a random 2D-sheet mixture of these cations. Fishman and Aharony have provided theoretical models for random alloys of two antiferromagnets with different periodicities, different anisotropies and different interactions in separate studies,¹⁻³ but their results cannot be directly applied to our system which represents a combination of all three forms of competition.

A solid solution of analogous sulfides, on the other hand, results in a spin glass state at intermediate compositions.⁷ Both MnPS_3 and FePS_3 order antiferromagnetically with spins normal to colored the ab plane and $k = [000]$ and $k = [01\frac{1}{2}]$, respectively. In MnPS_3 , each Mn^{2+} is antiferromagnetically coupled with its nearest neighbors in the plane and there is ferromagnetic coupling between the planes. In FePS_3 , each Fe^{2+} is ferromagnetically coupled with two nearest neighbors and antiferromagnetically with the third one and forms zigzag spin chains coupled antiferromagnetically within each layer. MnPS_3 is magnetically isotropic with a very small $D = 0.105$ K, with exchange interactions of $J_1 = -9.1$ K, $J_2 = -0.83$ K and $J_3 = -2.15$ K.³³ The nature of small anisotropy is debated between dipolar anisotropy and single ion anisotropy, however only its magnitude is relevant to our comparison. FePS_3 , on the other hand, is anisotropic with $D = 31.7$ K, approximately double the exchange parameters: $J_1 = 17.4$ K, $J_2 = -0.48$ K, $J_3 = -11.4$ K.³⁴ The sulfides form a spin glass when mixed randomly because competing antiferromagnetic and ferromagnetic exchange interactions within the planes are frozen without long-range preference for specific orientations (small D).^{7,35} The local Mn^{2+} symmetries of MPS_3 and MPSe_3 compounds both contain trigonally-distorted octahedra, with deviations about $3-4^\circ$ and 5° , respectively, and short/long bond distances of $2.70/2.74$ Å and $2.62/2.63$ Å, respectively.^{10,36} Formally, the site symmetry is actually higher for the selenide (C_3 versus C_2) as a consequence of the interlayer stacking. Small differences in local symmetry are not expected to dominate magnetic anisotropy, although systematic theoretical and computational work could shed additional light on the magnitude of these effects.

In contrast to the sulfide analogs, the absence of a spin glass state in $\text{Mn}_{1-x}\text{Fe}_x\text{PSe}_3$ can be explained by the dominance of anisotropies D_{Mn} and D_{Fe} over the exchange interactions. The tendency to obey a particular magnetic ordering increases with increasing anisotropy. Even small local chemical clustering in a randomly mixed solid solution can change the spin dynamics and segregate the system into coexisting magnetic domains of the

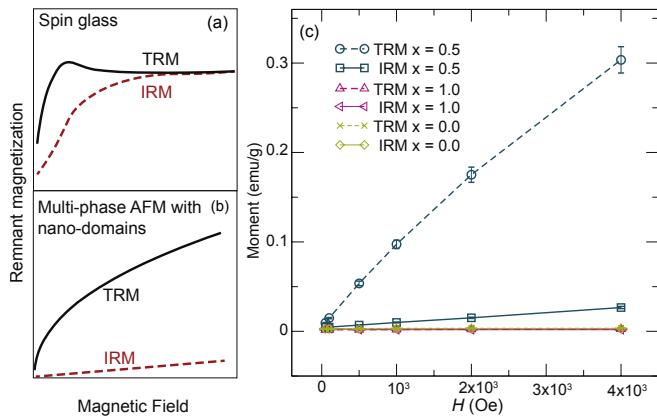


Figure 10. Schematic figure of thermoremanent magnetization (TRM) and isothermal remanent magnetization (IRM) for (a) spin glass, (b) nano-wires, adapted from article by Benitez et. al.³⁷, (c) Thermoremanent magnetization (TRM) of $x = 0.5$ samples shows an sub-exponential increase with field and divergence from isothermal magnetization (IRM), typical of an antiferromagnetic system with small domains and polarizable domain walls. The end members MnPSe_3 and FePSe_3 show no remanence.

avored end members. Local regions rich in Mn^{2+} or Fe^{2+} type ions can continue to polarize the magnetic ordering in their vicinity resulting in a two-phase competition region between $x = 0.25$ and $x = 0.875$.

Among the SG and 2-phase models that are possible ground states for such randomly-mixed 2D systems, each has its own tendency for formation based on J and D competition. The macroscopic response of these scenarios manifest in changes in the amount of uncompensated spins and their time-dependent susceptibility. Clearly, the spin glass scenario is ruled out of $\text{Mn}_{1-x}\text{Fe}_x\text{PSe}_3$ due to the high amount of ordered moment observed in the neutron diffraction data, but additional confirmation can be seen in time-dependent magnetization measurements.

Thermoremanent magnetization (TRM) and isothermal remanent magnetization (IRM) curves for ideal bulk antiferromagnets should be zero,³⁸ and higher values of TRM versus IRM denote irreversibility as embodied in a spin-glass (evenly-distributed frozen spins) or nano-domain behavior with a large fraction of uncompensated surfaces, occasionally seen in core-shell nanoparticles. Both behaviors are shown schematically in Figure 10.³⁷ For a spin glass, the IRM increases with increasing field, then meets the TRM curve at moderate field values, where both then saturate. The TRM also exhibits a characteristic peak at intermediate fields. TRM-IRM curves for antiferromagnetic nanoparticles have been measured and show an increasing TRM and IRM with no signs of saturation, a behavior that has been often compared to a 2D-DAFF response.³⁹

The TRM and IRM measurements at 5 K on $\text{Mn}_{1-x}\text{Fe}_x\text{PSe}_3$ for $x = 0.0, 0.5, 1.0$ are shown in Figure 10. TRM and IRM for $x = 0.0$ and 1.0 are negligible

(ideal bulk antiferromagnets) as compared to those for $x = 0.5$. For $x = 0.5$, the IRM increases nearly linearly, but at a slower rate than TRM. TRM and IRM for $x = 0.5$ does not saturate at high magnetic fields and does not display a spin-glass behavior, but instead matches interface-dominated behavior, which is seen in systems with small magnetic domain sizes, for example in Co_3O_4 nanowires, where uncompensated surface spins lead to irreversibility in addition to the regular antiferromagnetic contribution from the wires.³⁹ The decrease in correlation lengths of coexisting clusters of MnPSe_3 and FePSe_3 type ordering at intermediate compositions lead to more “uncompensated surfaces” with random ordering, which results in an increasing TRM and IRM.

The final magnetic phase diagram of $\text{Mn}_{1-x}\text{Fe}_x\text{PSe}_3$ is shown in Figure 11. The phase transition lines were drawn based on T_{max} obtained from $\chi-T$ measurements. Between $x = 0.0$ and $x = 0.25$, MnPSe_3 type magnetic ordering is present with introduction of short range correlations as x or Fe^{2+} concentration is increased. T_{max} decreases as x increases and is minimum for $x = 0.5$. Between $x = 0.25$ and $x = 0.875$, mixed ordering or coexistence of Mn^{2+} - and Fe^{2+} -type ordering is present. The mixed phase forms nano-sized chemically disordered clusters which display both kinds of ordering. The uncompensated surfaces between the clusters increase as the cluster size decreases and the effect can be seen in TRM-IRM, ZFC-FC magnetization and neutron diffraction measurements. Cluster size decreases as a function of chemical disorder present and is smallest for $x = 0.5$. The absence of Schottky anomaly in heat capacity for $x = 0.5$ suggests short range ordering where the transition lines in the phase diagram defined by T_{max} over intermediate compositions are not smooth and very well defined. For $x > 0.875$, FePSe_3 type magnetic ordering is present. The strong dependence of correlation lengths on the Fe^{2+} concentration for $x > 0.5$ suggests a lower value of anisotropy D_{Fe} as compared to D_{Mn} . This is also supported by weak dependence of correlation lengths on Fe^{2+} concentration for $x < 0.5$.

IV. CONCLUSIONS

In conclusion, we have established a magnetic phase diagram of a mixed spin, mixed interaction, mixed anisotropy and mixed periodicity system $\text{Mn}_{1-x}\text{Fe}_x\text{PSe}_3$ using a combination of X-ray diffraction, X-ray Fluorescence, neutron diffraction, DC magnetic susceptibility, TRM, IRM and heat capacity measurements on bulk powder samples. This is the first solid solution study of a random magnet system in metal selenophosphates family. Both kinds of MnPSe_3 and FePSe_3 type ordering are found to co-exist at intermediate compositions in the form of nanosized clusters. FePSe_3 type ordering is found to be more susceptible to doping as compared to the MnPSe_3 type ordering. A long range ordering does not take place in intermediate compositions upto 1.5 K

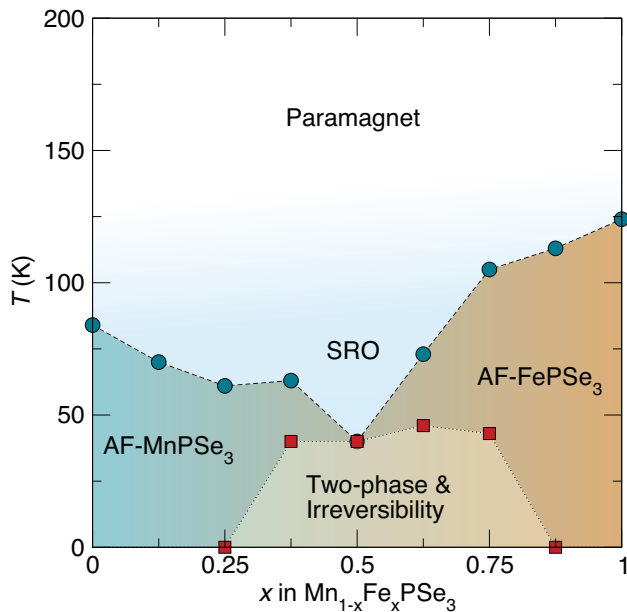


Figure 11. Magnetic phase diagram of $\text{Mn}_{1-x}\text{Fe}_x\text{PSe}_3$ showing three regions with MnPSe_3 -type, mixed-type and FePSe_3 -type AFM ordering. The circles represent T_{max} from $\chi - T$ measurements and a crossover from paramagnetic state to a magnetic state, while the two-phase competition region is best denoted by the susceptibility T_{split} (squares). Short-range order (SRO) is evident from deviation from Curie-Weiss susceptibility and diffuse magnetic nuclear scattering intensity.

and the broad diffuse scattering peaks are observed in neutron diffraction patterns. The magnetic ordering in intermediate compositions take place over a wide temperature range and does not display a characteristic lambda anomaly in heat capacity. The uncompensated surface spins increase with shorter correlation lengths and are evident in DC magnetization and TRM-IRM measurements. The mixed ordering can be explained by high values of D arising from ligand spin-orbit contributions. Future measurements involving single crystal neutron diffraction can be employed to establish the direction of moments withing the basal plane in MnPSe_3 . Magnetic domain imaging such as lorentz microscopy and magnetic force microscopy can be used to further characterize and image the anisotropic nature of the domains.

ACKNOWLEDGMENTS

We acknowledge support from the Center for Emergent Superconductivity, an Energy Frontier Research Center funded by the U.S. Department of Energy, Office of Science, Office of Basic Energy Sciences under Award Number DEAC0298CH1088. Magnetic and heat capacity measurements were carried out in part in the Materials Research Laboratory Central Research Facilities, University of Illinois. Neutron powder diffraction measurements conducted at ORNL's High Flux Isotope Reactor was sponsored by the Scientific User Facilities Division, Office of Basic Energy Sciences, US Department of Energy.

- ¹ S. Fishman and A. Aharony, Phys. Rev. B **18**, 3507 (1978).
- ² S. Fishman and A. Aharony, Phys. Rev. B **19**, 3776 (1979).
- ³ S. Fishman and A. Aharony, Phys. Rev. B **21**, 280 (1980).
- ⁴ A. Pirogov, J.-G. Park, A. Ermolenko, A. Korolev, A. Kuchin, S. Lee, Y. Choi, J. Park, M. Ranot, J. Yi, *et al.*, Phys. Rev. B **79**, 174412 (2009).
- ⁵ P.-z. Wong, Phys. Rev. B **34**, 1864 (1986).
- ⁶ F. Wegner, Solid State Commun. **12**, 785 (1973).
- ⁷ Y. Takano, A. Arai, Y. Takahashi, K. Takase, and K. Sekizawa, J. Appl. Phys. **93**, 8197 (2003).
- ⁸ E. Ressouche, M. Loire, V. Simonet, R. Ballou, A. Stunault, and A. Wildes, Phys. Rev. B **82**, 100408 (2010).
- ⁹ C. Friedel, "Thiohypophosphates," (1894).
- ¹⁰ A. Wiedenmann, J. Rossat-Mignod, A. Louisy, R. Brec, and J. Rouxel, Solid State Commun. **40**, 1067 (1981).
- ¹¹ A. A. Coelho, A Computer Programme for Rietveld Analysis (2004).
- ¹² J. Rodriguez-Carvajal, in *Satellite meeting on powder diffraction of the XV congress of the IUCr*, Vol. 127 (Toulouse, France:[sn], 1990).
- ¹³ A. Wills, Physica B **276**, 680 (2000).
- ¹⁴ P. Joy and S. Vasudevan, Phys. Rev. B **46**, 5425 (1992).
- ¹⁵ S. Yusuf, A. K. Bera, N. S. Kini, I. Mirebeau, and S. Petit, Phys. Rev. B **82**, 094412 (2010).
- ¹⁶ A. Bera, S. Yusuf, A. Kumar, and C. Ritter, Phys. Rev. B **95**, 094424 (2017).
- ¹⁷ J. Lynn, T. Clinton, W. Li, R. Erwin, J. Liu, K. Vandervoort, and R. Shelton, Phys. Rev. Lett. **63**, 2606 (1989).
- ¹⁸ P. Jernberg, S. Bjarman, and R. Wäppling, Journal of magnetism and magnetic materials **46**, 178 (1984).
- ¹⁹ Q. Pei, X. Luo, G. Lin, J. Song, L. Hu, Y. Zou, L. Yu, W. Tong, W. Song, W. Lu, *et al.*, J. Appl. Phys. **119**, 043902 (2016).
- ²⁰ D. Lançon, H. Walker, E. Ressouche, B. Ouladdiaf, K. Rule, G. McIntyre, T. Hicks, H. M. Rønnow, and A. Wildes, Phys. Rev. B **94**, 214407 (2016).
- ²¹ E. Granado, J. W. Lynn, R. F. Jardim, and M. S. Torikachvili, Phys. Rev. Lett. **110**, 017202 (2013).
- ²² M. Saes, N. Raju, and J. Greedan, J. Solid State Chem. **140**, 7 (1998).
- ²³ N. Ni, E. Climent-Pascual, S. Jia, Q. Huang, and R. Cava, Phys. Rev. B **82**, 214419 (2010).
- ²⁴ B. E. Warren, Phys. Rev. **59**, 693 (1941).
- ²⁵ P. Jeevanandam and S. Vasudevan, J. Phys. Condens. Mat. **11**, 3563 (1999).
- ²⁶ H. Hoekstra, P. Boudewijn, H. Groenier, and C. Haas, Physica B+C **121**, 62 (1983).
- ²⁷ C. Ronda, H. Siekman, and C. Haas, Physica B+C **144**, 331 (1987).
- ²⁸ S. R. Chowdhury and S. Mishra, Physical Chemistry Chemical Physics **19**, 16914 (2017).

- ²⁹ J. L. Lado and J. Fernandez-Rossier, 2D Materials **4**, 035002 (2017).
- ³⁰ E. Lhotel, V. Simonet, E. Ressouche, B. Canals, D. B. Amabilino, C. Sporer, D. Luneau, J. Veciana, and C. Paulsen, Physical Review B **75**, 104429 (2007).
- ³¹ T. Sato, H. Kadowaki, and K. Iio, Physica B: Condensed Matter **213-214**, 224 (1995).
- ³² R. G. Barnes and W. V. Smith, Physical Review **93**, 95 (1954).
- ³³ A. Wildes, B. Roessli, B. Lebech, and K. Godfrey, J. Phys. Condens. Mat. **10**, 6417 (1998).
- ³⁴ D. Lancon, H. Walker, E. Ressouche, B. Ouladdiaf, K. Rule, G. McIntyre, T. Hicks, H. M. Rønnow, and A. Wildes, Phys. Rev. B **94**, 214407 (2016).
- ³⁵ T. Masubuchi, H. Hoya, T. Watanabe, Y. Takahashi, S. Ban, N. Ohkubo, K. Takase, and Y. Takano, J. Alloys Compd. **460**, 668 (2008).
- ³⁶ G. Ouvrard, R. Brec, and J. Rouxel, Materials Research Bulletin **20**, 1181 (1985).
- ³⁷ M. Benitez, O. Petravic, H. Tüysüz, F. Schüth, and H. Zabel, Phys. Rev. B **83**, 134424 (2011).
- ³⁸ K. L. S. Rodríguez, M. Hoffmann, F. Golmar, G. Pasquevich, P. Werner, W. Hergert, and C. E. R. Torres, Appl. Surf. Sci. **393**, 256 (2017).
- ³⁹ M. Benitez, O. Petravic, E. Salabas, F. Radu, H. Tüysüz, F. Schüth, and H. Zabel, Phys. Rev. Lett. **101**, 097206 (2008).